

HEAT TRANSFER CHARACTERISTICS AND VELOCITY MEASUREMENTS OF MAIN FLOW IN A RECTANGULAR CHANNEL WITH TWO RIBBED-WALLS

By

Prof. Abdalla S. Hanafi
Cairo University

Ass. Prof. Karam M. El-Shazly
Zagazig University, Shoubra

Ass. Lect. Aly A. Abdel Aziz
Zagazig University, Shoubra

ABSTRACT

An optimal rib geometry was investigated experimentally and numerically in the present work to give an enhancement of heat transfer coefficient and fluid flow characteristics at equal mass flow rate and pumping power constraints through the cooling passage. Two different rib shapes (grooved square and inverted trapezoidal) were conducted to investigate its effects on the fluid flow and heat transfer characteristics. The experimental correlations of the average Nusselt number ratio (\overline{Nu}/Nu_s) with different rib shapes are developed in terms of Reynolds number and rib pitch in eq. (1).

$$\overline{Nu}/Nu_s = a.Re^{-0.10264}.(p/e)^{-0.208} \quad (1)$$
$$(2.3 \times 10^4 \leq Re \leq 5.6 \times 10^4, \dots, 10 \leq p/e \leq 40)$$

The constant coefficient (a) in eq. (1) is equal to 12.28 and 13.16 for grooved square and inverted trapezoidal ribs, respectively, where the maximum deviation errors are $\pm 11\%$ and $\pm 16\%$. The combined effects of rib pitch, rib shape, and rib alignment on the heat transfer coefficient for fully developed turbulent flow within a rectangular duct with two opposite ribbed-walls were determined. The rib pitch to height ratios were 10, 20, and 40; the rib height to duct hydraulic diameter and duct height ratios are kept at 0.081 and 0.125 respectively. A full field measuring technique was used to measure the velocity vectors magnitude and direction. ANSYS FLOTTRAN CFD computer code (1997) was applied to predict the flow pattern velocity and heat transfer coefficient to support the experimental results. The results show that heat transfer performance of grooved square and inverted trapezoidal ribs is much better than the ribbed-duct with solid square rib at same base heat transfer area and rib height. A comparison between the experimental and computational results and also with the previous results was investigated where good agreement was found between them.

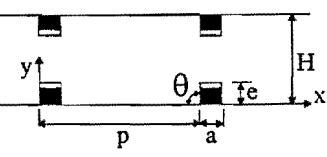
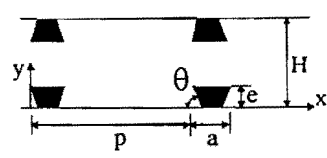
KEYWORDS

Turbulent heat transfer, Ribbed-duct, Rib geometry, Velocity measurement, ANSYS CFD.

INTRODUCTION

Heat transfer characteristics in channels or pipes with solid-type rib-roughened walls have already been extensively investigated. However, the increase in heat transfer is accompanied by an increase of the resistance to the fluid flow. Some investigations have been conducted toward establishing an optimal rib geometry, which gives the best heat transfer performance for a given pumping power or flow rate. Relevant geometric parameters discussed in previous works are channel aspect ratio (Hong et al 1993), rib angle of attack (Han et al 1991), rib spacing (Liou and Hwang 1992 part1), rib shape (Liou and Hwang 1992 part2), and blockage ratio (e/D_e), (Han 1984). Until 1991, the numerical simulation of turbulent flow through a channel of one ribbed-wall is made of a fixed rib geometry, and the effect of the rib spacing and rib height on the distributions of local heat transfer coefficient have not been investigated. Therefore, in the present work (ANSYS FLOTTRAN CFD 1997) code is used to determine numerically the hydrodynamic effect of rib shape on the heat transfer and flow characteristics for forced convection through a channel with two opposite roughened walls. An optical technique was used to measure the velocity distributions of air flow in the test field around rib. Table 1 shows briefly the rib shapes, rib pitches, and coordinate system used in the present experimental work.

Table 1: Rib geometry and coordinate system used in the present experimental work.

Rib Geometry	H (mm)	e. (mm)	a. (mm)	p/e	θ	Shape
Grooved Square	40	5.2	5.2	10	90°	
				20		
				40		
Inverted Trapezoidal	40	5.2	7.0	10	83°	
				20		
				40		

N.B. Test section has 46, 22, and 10 ribs at $p/e = 10, 20$, and 40, respectively, $Re = 23,000$ to 56,000, $e/D_e = 0.081$.

EXPERIMENTAL INVESTIGATION

The schematic diagram of flow system and overall arrangement of optical technique are illustrated in Figs. 1 and 2, respectively. The flow system consists of: air blower, orifice flow meter, transition duct, straightener, test section, main entrance duct, and bell mouth intake duct. The air blower is of the centrifugal type. An AC coupled motor of 3 HP drives it. The airflow discharge is controlled at the outlet of the air blower by means of a variable area outlet gate. A special apparatus was designed and built for velocity measurements. A 650-Watt Halogen source provides a high dense light. The light beams transferred through a cylinder of 52 mm length and have a convex lens of diameter 41.6 mm, and then the beams are concentrated in a single spot. The object beams then pass to the test section through a

fiber optical cable of 3.9 mm diameter and 1000 mm length. This fiber optical cable consists of a large number of optical fibers with about 4 μm diameter. One end of the optical fibers cable has a finite lens of diameter 4.15 mm, the other free end of optical fibers cable is glued on a very thin strip of thickness 0.5 mm and dimension 5 \times 20 mm to provide a light sheet of thickness 4 μm approximately. The airflow is seeded with artificial scatters, which were provided to the light sheet emanating from optical fibers. Thus the fluid velocity could be determined from the predicted particle velocity. These particles size is small enough and the particle velocity is expected to be close to the fluid velocity.

TEST SECTION

The test section consists of two principle ribbed-walls and two side smooth walls. It was 1200 mm in length and had a rectangular cross section 160 mm (aluminum plate) \times 40 mm (plexiglas) (z-y plane) i.e., having aspect ratio equal to 4. The channel aspect ratio of 4 used in the present work is the same aspect ratio employed by (Liou and Hwang 1992 part2) for the studies of rib roughness channel flows. The sidewalls of the entire test section are made of Plexiglas plates (8 mm thick) to provide good view for spatial optical technique measurements. Detailed construction of the test section is shown in **Fig. 3a** and **Fig. 3b**. **Fig. 4** shows the grooved rib geometry used in the present work. Two heating units of thickness (70 mm) emit heat to the top and bottom walls of the test section, respectively. Each heating unit was adhered uniformly to the aluminum plate and could be controlled individually by a voltage regulator to give constant heat flux along the entire test section. Copper-constantan thermocouples (having about 0.2 mm wire diameter) were used to measure the local wall temperature of the aluminum plate and the rib surface. About eighty-eight thermocouples for the fully developed region are distributed between x/D_e from 11.7 to 15.6 (along the mid-span and spanwise direction of the heating plate) to measure the temperature used to calculate the local heat transfer coefficient of the ribbed-duct as shown in **Fig. 5**. About twelve thermocouples are distributed on the rib surface at $x/D_e = 12.5$. Two thermocouples were used to measure air temperature entering and leaving the test channel. About 33 thermocouples were attached to the backside and edges of the heating plate and main heater to measure the outer wall temperature of the test section for calculation the heat loss. Velocity vectors in magnitude and directions were calculated from the flow traces of seeding particles through the airflow. The fiber optical cable provided the mid-span of the ribbed-wall by a light sheet from a 650-Watt Halogen lamp. A video camera with a shutter time of 1/30 second was used to view and record the scattering light from the seeding particles through the ribbed-duct with different rib shapes. An instantaneous photography of the velocity distributions was monitored and recorded on a videocassette recorder for storage and further image processing. The output video pictures were feed into a personal computer for storage and analysis. The capture trace of the seeding particles was then printed using laser jet printer. The local heat transfer coefficient was calculated from the heat flux (q) transferred per unit area from the wall to the cooling air and divided by the difference between the local wall temperature (T_{wx}) and the local mean bulk air temperature (T_{bx}) as follows:

$$h(x) = q / (T_{wx} - T_{bx}) \quad (2)$$

The average heat transfer coefficient (h) for the periodically fully developed region was calculated in terms of the average wall temperature (\bar{T}_w) as follows:

$$h = q / (\bar{T}_w - \bar{T}_b) \quad (3)$$

where \bar{T}_w is the average wall temperature in one rib pitch, and \bar{T}_b is the average mean bulk air temperature that is evaluated as following:

$$\bar{T}_b = \int_0^{L_h} \frac{T_{bx}}{L_h} dx \quad (4)$$

where L_h is the wetted length of heated ribbed-wall in one rib pitch.

The average Nusselt number, Nu , is determined in terms of the average wall temperature (\bar{T}_w) as:

$$\bar{Nu} = q.De/[k_f(\bar{T}_w - \bar{T}_b)] \quad (5)$$

where k_f is the thermal conductivity of air flow, which was calculated at average film temperature (T_f), $T_f = (\bar{T}_w + \bar{T}_b)/2$. The friction factor in the fully developed region was calculated from the pressure drop across the flow duct by pressure taps located at the bottom ribbed wall and mass flow rate of the air as follows:

$$f = \frac{(\Delta p / \Delta x) De}{2 \rho u_m^2} \quad (6)$$

EXPERIMENTAL RESULTS

The vector plot in Fig. 6 shows the full field measured velocity around the ribs for asymmetric ribbed-duct (One ribbed-wall) with different rib shapes for ($p/e=10$, $e/D_e=0.081$). Flow contraction upstream the rib and expansion downstream the rib can be seen for fully developed flow with different rib shapes. It is observed also, that the rib accelerates the flow at a distance of $2.7e$ upstream the front face of rib approximately. The front rib edge breaks the boundary layer, which are reattached to the ribbed-wall at a reattachment length of $(5e)$ approximately, from the front face of rib and slightly depends on the rib shape. The velocity magnitude for $p/e=10$ have a small significant changes with different rib shapes where the inverted trapezoidal rib accelerates the flow more slightly than the square and trapezoidal ribs.

Smooth Duct Results

Before carrying out heat transfer measurements of ribbed-duct, the smooth rectangular duct measurements were carried out to normalize the present experimental results of ribbed-duct. Fig. 7 shows that the difference between the axial wall temperature and the bulk temperature has a constant value at $x/D_e \geq 5.62$. Fig. 8 shows higher values of Nusselt number at the leading edge of the duct inlet followed by a decrease approaching a nearly constant value at $x/D_e \geq 5.62$. Fig. 9 shows good agreement between the average Nusselt number for the present smooth rectangular duct and the results of fully developed turbulent flow through circular tube (Dittus-Boelter equation).

Thermal Flow Patterns

The temperature distributions in the test field around ribs through asymmetric ribbed-duct with solid and grooved square ribs are shown in Figs. 10a and 10b, respectively, for $p/e = 10$ and $Re = 26,583$. It can be seen that the isothermal contours on the upstream face of rib surface is thin while on the downstream face is thick. The grooves on rib surface accelerate the flow and the velocities in the test field around rib increase, so the thermal boundary layer decreases for the square grooved rib and the heat transfer coefficient increases.

Local Heat Transfer

Figure 11 illustrates variation of dimensionless local wall temperature distributions versus dimensionless axial distance for asymmetric ribbed-duct with solid square and grooved square rib types at constant value of Reynolds number ($Re = 39,209$) and rib pitch ($p/e = 10$). The grooved rib has lower wall temperature than the solid rib. The flow is accelerated through the groove and the heat is convected by the air flow through these grooves. Therefore, the grooved ribs provide heat transfer enhancement in comparison with the solid ribs by about 23 % as shown in Fig. 12 due to increasing the rib surface and the turbulent transport of high disturbance flow. Figures 13 and 14 show variations of the dimensionless local wall temperature and local Nusselt number ratio distributions versus dimensionless axial distance at different rib pitches for symmetric ribbed-duct (In-line arrangement) with square grooved rib and inverted trapezoidal rib, respectively at $Re = 39,700$. It can be seen that the local temperature distributions increase as the rib pitch increases, due to increasing of thermal boundary layer thickness and decreasing the frequency of flow acceleration. It is found that the local Nusselt number ratio increases as the rib pitch decreases and reaches a maximum value at $p/e = 10$, due to the high effective blockage and distortion which accelerate the flow. Figures 15 and 16 show the variations of dimensionless local wall temperature distributions and local Nusselt number ratios versus dimensionless axial distance for symmetric ribbed-duct with different rib shapes, respectively, ($Re = 40,000$, $p/e = 10$). The local temperature distributions for inverted trapezoidal rib have lower values on rib surface ($0.0 \leq x/e \leq 3.0$) than those for the square grooved rib. On the other hand, the square grooved rib has a lower values of dimensionless wall temperature than those of the inverted trapezoidal rib along the inter-distance between ribs at ($3.0 < x/e \leq 12.0$). For the different rib shapes, it is observed that the maximum local Nusselt number ratios are obtained nearest to the separation point (rib front tip) and the minimum value at the rear bottom rib corner. The low values of Nusselt number ratio is more likely to occur for the square grooved rib than the inverted trapezoidal rib at the rear rib face. This means that there is a close relation between the thermal behavior and aerodynamic behavior of flow, which had been investigated and described previously (Hanafi et al 2000). On the ribless wall, the square grooved rib has a higher local Nusselt number ratio than that of the inverted trapezoidal rib.

Average Nusselt Number

The average Nusselt number presented here is based on the numerical integration of local Nusselt number distributions between $x/D_e = 12.5-13.28$, $x/D_e = 12.5-14.0$, and $x/D_e = 12.5-15.62$ (one rib pitch, two rib pitches, and four rib pitches) for $p/e = 10$, 20, and 40, respectively. These plots of average Nusselt number ratios are used for performance comparison and correlations provision. Figures 17 and 18 show the effect of Reynolds number on the average Nusselt number ratio for two ribbed-walls with different rib alignments for square grooved ribs and inverted trapezoidal ribs, respectively. In case of square grooved rib, the average Nusselt number ratio decreases slowly with increasing

Reynolds number for in-line and staggered rib types. It also shows that the average Nusselt number ratio for symmetric ribbed-duct with square grooved rib is higher than that for the staggered ribbed-duct by 12 percent. **Figure 18** shows that there is no significant effect of rib alignment and Reynolds number on the average Nusselt number ratios for inverted trapezoidal rib shape. **Figure 19** shows effect of Reynolds numbers on the average Nusselt number ratio for asymmetric ribbed-duct with solid and grooved square ribs at a fixed rib pitch ratio of $p/e = 10$. It is found that for the range of Reynolds number, the heat transfer augmentations are about (1.8- 2.14) and (2.0 – 2.26) for solid and square grooved ribs, respectively, as compared with the smooth duct results. The grooved and solid rib shapes pay about 4 and 3.6 times the friction loss penalty of smooth duct, respectively. **Figure 20** shows the effects of rib shape, rib pitch, and Reynolds number on the average Nusselt number ratio under the two constraints of flow for turbulent fully developed flow through symmetric ribbed-duct. It can be concluded that at equal mass flow rate, the rib shape has a high significant effect on the average Nusselt number ratio. On the other hand, the rib shape has a low influence on the average Nusselt number ratio for equal pumping power constraint. The inverted trapezoidal rib shape has a higher heat transfer enhancement at $p/e = 20$ than that at $p/e = 10$ for equal pumping power constraint and nearly have the same enhancement at equal mass flow rate. **Figure 21** shows the dependency of average friction factor and Colburn heat transfer factor on the Reynolds number for turbulent flow through symmetric ribbed-duct with different rib shapes as well as different pitch to height ratios. The average friction factor and Colburn factor decrease with increasing Reynolds number. The Reynolds number effect on the Colburn factor is slightly stronger than the effect on the friction factor. The more flattest of f - Re curve than the J - Re curve indicates that the heat transfer augmentations occurs with low pumping power and becomes more significant at low Reynolds number values. **Figure 22** shows a comparison of average Nusselt number ratio between the present experimental correlations in eq. (1) and the previous correlations for different rib shapes ($p/e = 10$, $e/D_e = 0.081$). It can be seen that the heat transfer enhancement ($Nu/Nu_s > 1$) is attained with all of the rib shapes employed in the present work (Inverted trapezoidal rib and square grooved rib) and in the previous investigation of (Liou et al 1992 part2) (solid square rib, triangular rib, and semicircular rib). In the present used Reynolds number range, as compared with the smooth duct results, the increments of average heat transfer coefficient enhancement are about (173-186), (147-170), (99-123), (62-80), and (58-73) % for the inverted trapezoidal rib, the square grooved rib, the solid square rib, the triangular rib, and the semicircular rib, respectively. For fully developed turbulent flow through symmetric ribbed-duct with square grooved and inverted trapezoidal ribs, the average Nusselt number ratios (\overline{Nu}/Nu_s) can be further correlated by the power law in terms of Reynolds number (Re) and rib pitch to height ratio (p/e) as below:

$$\overline{Nu}/Nu_s = a \cdot Re^{-0.10264} \cdot (p/e)^{-0.208} \quad (7)$$

($2.3 \times 10^4 \leq Re \leq 5.6 \times 10^4$, $10 \leq p/e \leq 40$)

The constant coefficient (a) in eq. (7) is equal to 12.28 and 13.16 for grooved square and inverted trapezoidal ribs, respectively and the maximum deviations are ± 11 % and ± 16 %.

COMPUTATIONAL CODE RESULTS

ANSYS code is implemented to determine the periodic flow characteristic over ribbed-wall duct with different rib geometries. ANSYS FLOTTRAN program used the k - ϵ model because this turbulence model is useful in a general purpose CFD (Computational Fluid Dynamics)

code which is adequate for most applications. It is noted here that the grid elements used are denser in the two dimensional plane. Therefore, the computational advantages are obvious. All solutions apply a uniform velocity profile at inlet and zero velocity condition in the direction normal to the inlet flow. No-slip (zero velocity) conditions are applied all along the walls. Relative pressure parameters are zero at the duct outlet. The present work uses a model which has 32,650 elements that gives a reattachment length of ($x_1 = 4.4e$) which lies in the range of (Liou et al 1993). The two opposite walls (top and bottom plates) of the smooth duct are heated by a constant heat flux. **Fig. 23** shows that the heat transfer coefficient (accordingly Nusselt number) increases when the air-stream velocity (Reynolds numbers) increases. It can be seen from **Fig. 23** that there is good agreement between the present numerical results and the previous Dittus-Boelters experimental correlations with a maximum deviation of 5 %. **Figure 24** compares the computational and present experimental velocity vectors in the test field around rib mounted on one ribbed-wall with $p/e = 10$ and at different rib shapes. The flow acceleration begins at about 2.4 rib height upstream rib. The maximum velocity vector appeared at the rib front edge and at the mean core flow. The predicted reattachment point from computational results is in a good agreement with the experimental measurements at about 4.5 e. **Figure 25** compares measured and computed results of local Nusselt number ratio for fully developed turbulent flow through symmetric ribbed-duct with solid square ribs at $p/e = 10$, $Re = 27,313$ and at same rib height ratio ($e/D_e = 0.081$). It is clear that for the ribless wall, the measured and computed results are nearly coincide with maximum error of 6 %. Along the front rib surface, no agreement is found due to the complex flow region around rib where a local peak turbulent energy appears. The difference between them may be probably attributed partly to the inadequency of the basic assumption of near-wall treatment of the wall function made in the $k-\epsilon$ model in the near rib region and to the instrumentation measurements. **Figure 26** compares measured and computed results of average Nusselt number ratio for symmetric ribbed-duct with different rib shapes at $p/e = 10$, $Re = 27,313$, and at same mass flow rate. It is observed from computational results that, the average Nusselt number ratio decreases strongly with increasing in Reynolds number for solid square rib than that for inverted trapezoidal rib. Also, the average Nusselt number ratio for inverted trapezoidal rib has a higher value than that for the solid square rib. The present experimental results are in good agreement with those of computed results with a maximum deviation error of 6 %. At same rib height ratio ($e/D_e=0.081$), a maximum deviation error of 17 % was found between the present computed results and the experimental results of (Liou et al 1992 part2) for solid square rib at $p/e = 10$.

CONCLUSIONS

The experimental results of heat transfer for the two ribbed-walls of channel show the following :-

1. Grooved ribs provide heat transfer enhancement in comparison with the solid ribs by 23 percent.
2. The rib alignment has a higher significant effect at the ribless-wall for square grooved-rib than that for inverted trapezoidal rib.
3. The local temperature distributions have lower values on the inverted trapezoidal rib surface than that on the square grooved-rib.
4. The low values of Nusselt number ratio is more likely to occur for the square grooved rib than that for the inverted trapezoidal rib.
5. The square grooved rib increases the average Nusselt number ratio approximately, 2.66-2.45, 2.46-2.26, and 2-1.86 times over those of smooth duct for $p/e = 10, 20$, and 40, respectively.

6. The heat transfer augmentations of square grooved rib are about (2.45-2.66) and (1.2-1.26) times that of the smooth duct and solid square rib, respectively.
7. The inverted trapezoidal rib shape has a higher heat transfer enhancement at $p/e = 20$ than that at $p/e = 10$ for same pumping power constraint, this is reversed for same mass flow rate constraint.
8. For square grooved rib, the Reynolds number has a higher significant effect on the average Nusselt number ratio than that for inverted trapezoidal rib for same mass flow rate.
9. The inverted trapezoidal rib increases the average Nusselt number ratio about 2.79-2.6, 2.77-2.55, and 2.05-1.788 times over those of smooth duct for $p/e = 10, 20$, and 40, respectively.
10. Rib shape has a high significant effect on the local heat transfer coefficient on rib surface and the heat transfer enhancement depends strongly on the turbulent transport which is influenced by the rib shape than the frequency of flow acceleration.

REFERENCES

ANSYS (1997), CFD FLOTRAN Analysis Guide, ANSYS, Inc.

Dittus F. W., and Boeltes, L.M.K. (1930), Publications on Engineering. University of California, Berkely, Vol. 2, p 443.

Hanafi A. S., El-Shazly K. M., and Abdel-Aziz A. A. (2000), Experimental and Numerical Investigation of Flow Characteristics in a Rectangular Channel With Two Ribbed-Walls, 11th International Mechanical Power Engineering Conference, Cairo, Feb (5-7), Vol. 2, pp F69-F88.

Hong, Y. J. Hsieh S. S. (1993), Heat Transfer and Friction Factor Measurements in Ducts With Staggered and in-Line Ribs. Transactions of the ASME, Vol. 115, February.

Han J. C., Zhang Y. M., and Lee C. P. (1991), Augmented Heat Transfer in Square Channels With Parallel, Crossed, and V-Shaped Angled Ribs, Transactions of the ASME, August, Vol. 113, PP. 590-596.

Han J.C. (1984), Heat Transfer and Friction in Channels With Two Opposite Rib-Roughened Walls, Transactions of the ASME, Vol. 106, pp. 774-781.

Liou T. M. and Hwang J. J. (1992 part1), Turbulent Heat Transfer augmentation and Friction in Periodic Fully Developed Channel Flows. Transactions of the ASME, Vol. 114, February 1992, pp. 56-64.

Liou T. M and Hwang J. J. (1992 part2), Effect of Ridge Shapes on Turbulent Heat Transfer and Friction in a Rectangular Channel. Int. J. Heat Mass Transfer, Vol. 36, No. 4, pp. 931-940.

Liou T. M., Hwang J. J., and Chen S. H. (1993), Simulation and measurement of enhanced turbulent heat transfer in a channel with periodic ribs on one principal wall, Int. J. Heat Transfer, Vol. 36, No. 2, pp. 507-517.

NOMENCLATURE

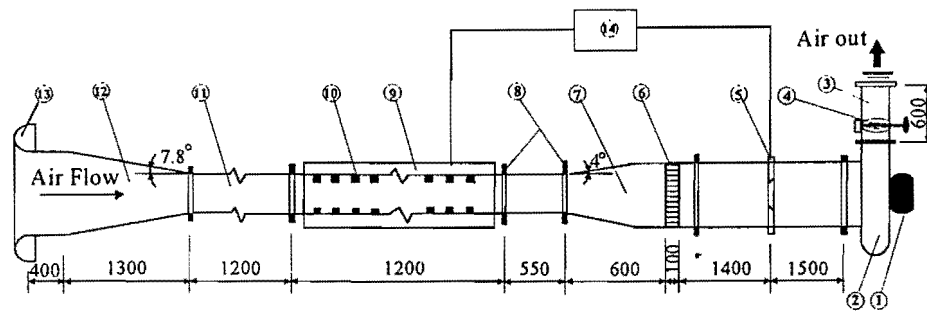
a.	- rib width, m
De	-hydraulic diameter, m
e.	-rib height, m
f	-average friction factor
h	- heat transfer coefficient, W/m ² .K
H	-channel height, m
L_h	-wetted length of heated ribbed-wall in one rib pitch, m
\overline{Nu}	- Average Nusselt number
Nu_s	- Average Nusselt number of smooth duct
p.	-rib pitch, m
p_d	- dynamic pressure, $(0.5\rho u_m)$, Pa
Δp	- pressure drop across the flow channel, Pa
q	- local wall heat flux, W/m ²
Re	-Reynolds number, $(\rho u De/\mu)$
$\overline{T_b}$	- average temperature of bulk mean air temperature, °C
T_{bx}	- local bulk mean air temperature, °C
$\overline{T_w}$	- average wall temperature of the heated plate and ribs, °C
T_{wx}	- local wall temperature of the heated plate and ribs, °C
u_m	-axial mean velocity upstream the ribbed-duct, m/s
x	-streamwise coordinate, m
x_l	-reattachment length, m
Δx	- axial distance, m
y	-transverse coordinate, m
z	-spanwise coordinate, m

Greek Symbols

θ	-angle intercept between the front face of rib and channel wall, deg.
μ	-dynamic viscosity, kg/m.s
ρ	-density, kg/m ³

Subscripts

d.	-dynamic
s	-smooth
l	- impingement point



- | | |
|-------------------------|------------------------------|
| 1. A.C electric motor. | 8. Flanges. |
| 2. Air blower. | 9. Test section. |
| 3. Exit duct. | 10. Ribs. |
| 4. Air gate controller. | 11. Main duct. |
| 5. Flow orifice meter. | 12. Contraction duct (10:1). |
| 6. Straightener. | 13. Bell-mouth intake. |
| 7. Transformation duct. | 14. Micro-manometer. |

Fig. 1: Schematic diagram of the test rig.

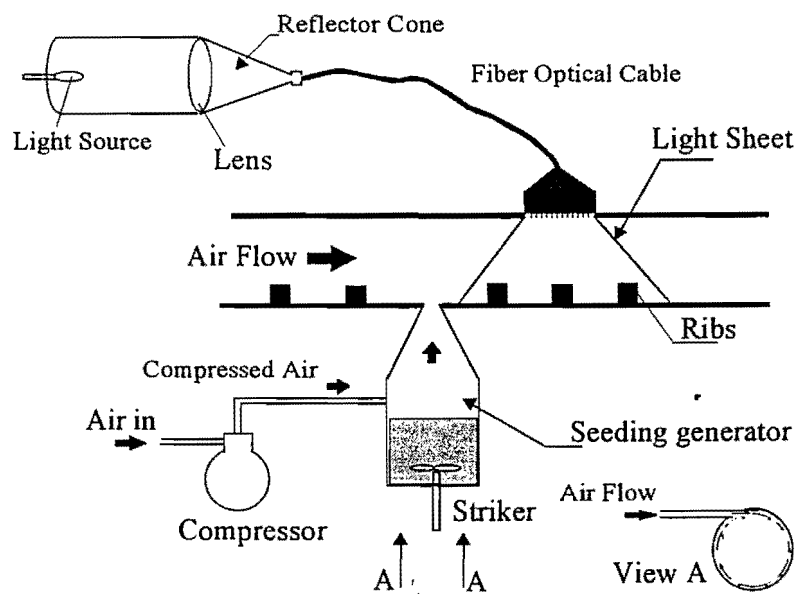
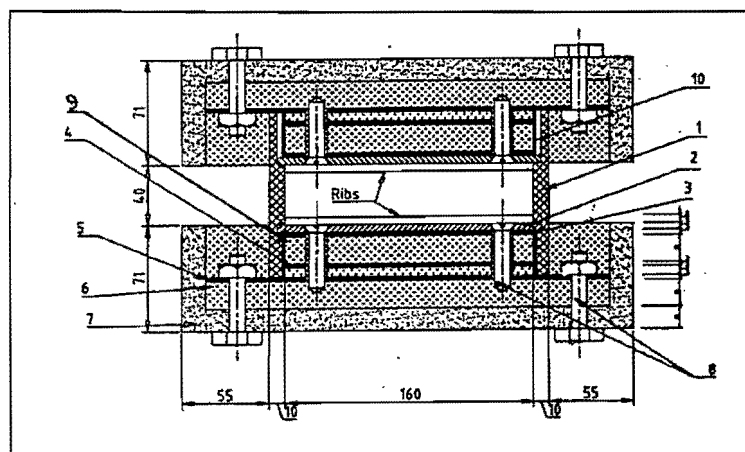
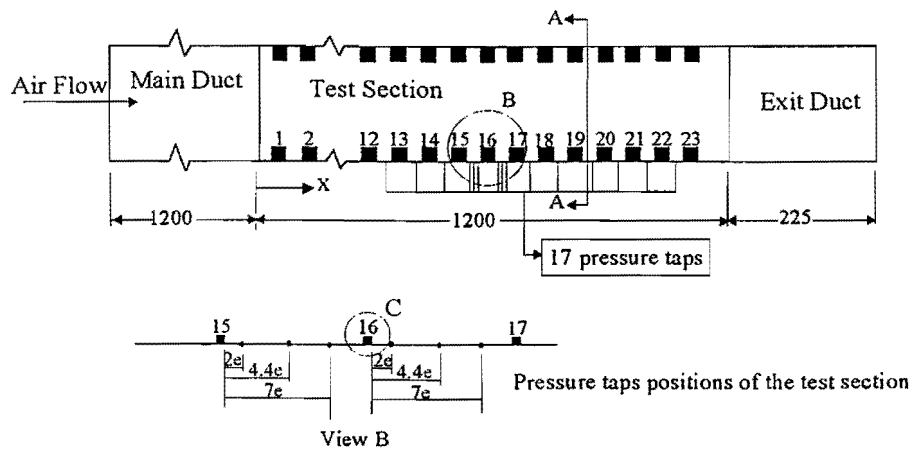


Fig. 2: Overall arrangement of spatial optical technique



- | | |
|---------------------|---------------------------------|
| 1. plexiglas. | 6. Asbestos insulation. |
| 2. Aluminum plate. | 7. Wooden frame. |
| 3. Main heater. | 8. Fixation and assembly parts. |
| 4. Guard heater. | 9. Heaters edge insulation |
| 5. Backelite sheet. | 10. Wires gap inside the frame. |

Fig. 3b: Cross section details at section A-A

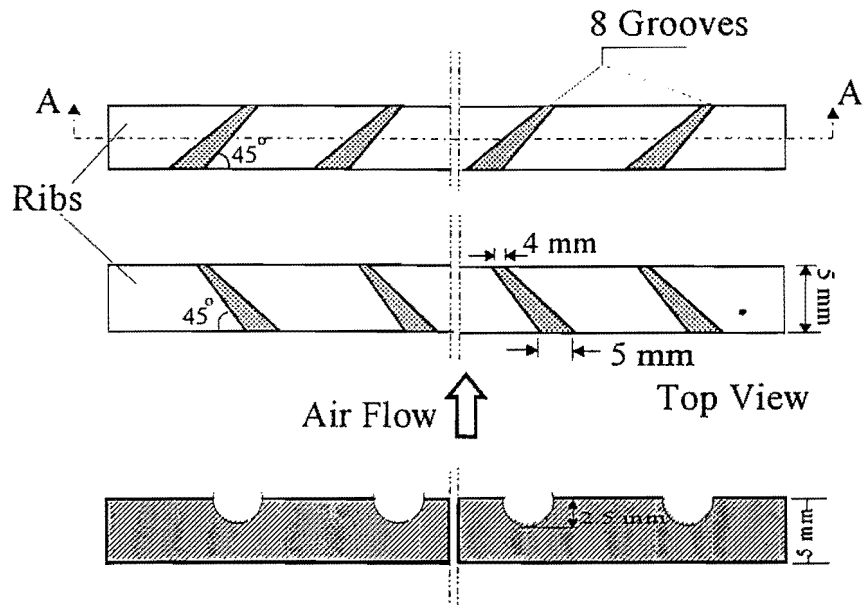


Fig. 4: Schematic diagram of grooved-ribs.

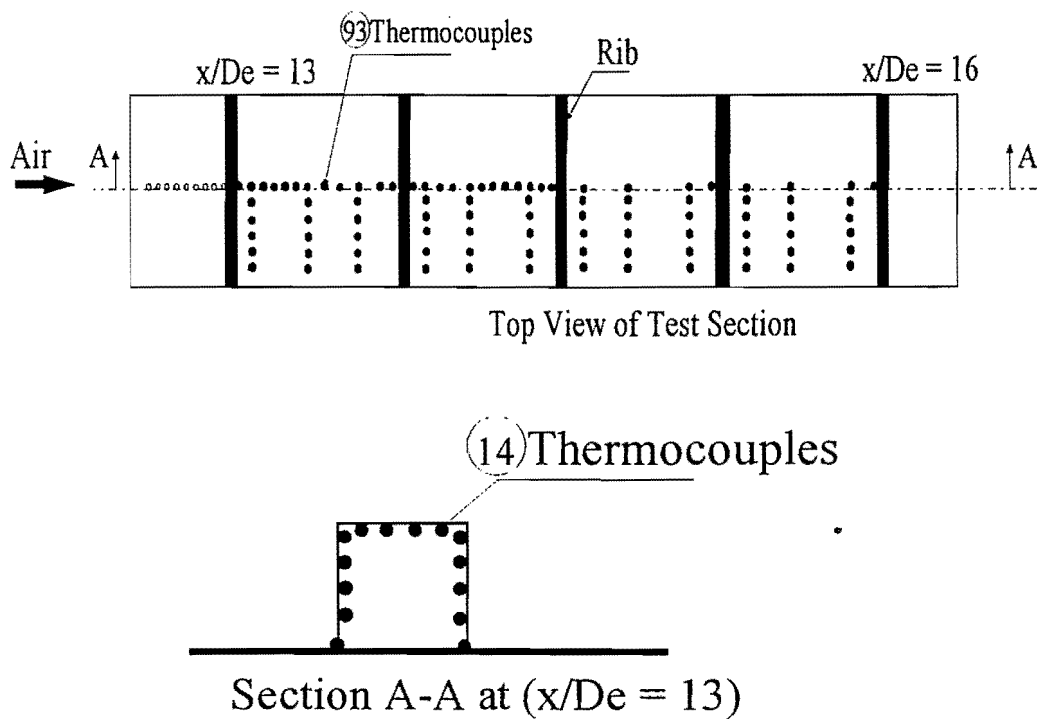


Fig. 5: Thermocouple locations on the bottom ribbed-wall and on the rib number (16) for fully developed region

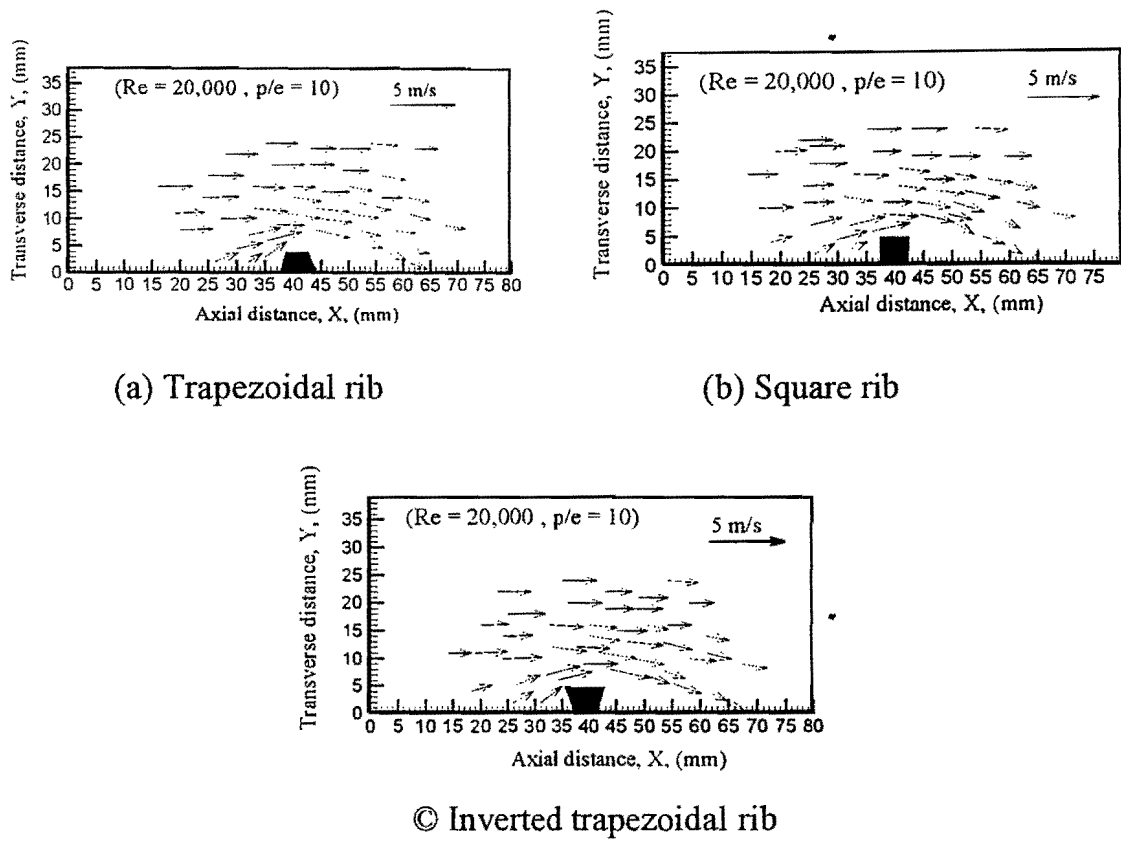


Fig. 6: Velocity distributions in the test field around rib with different rib shapes, ($p/e = 10$, $Re = 20,000$, $e/D_e = 0.081$).

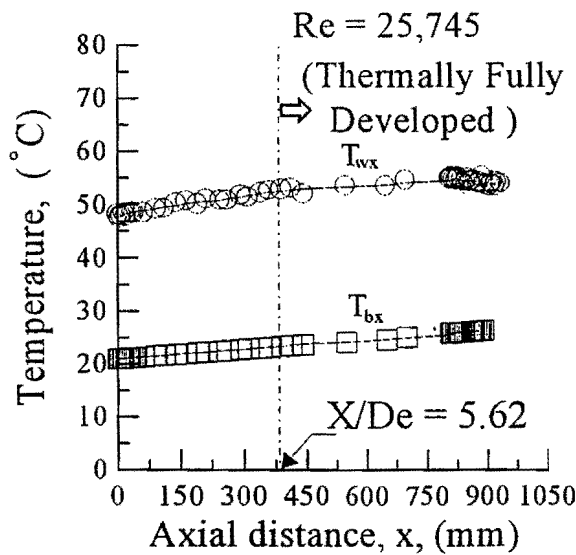


Fig. 7: Local wall and bulk temperature variations of smooth wall versus axial distance, $Re = 25,745$.

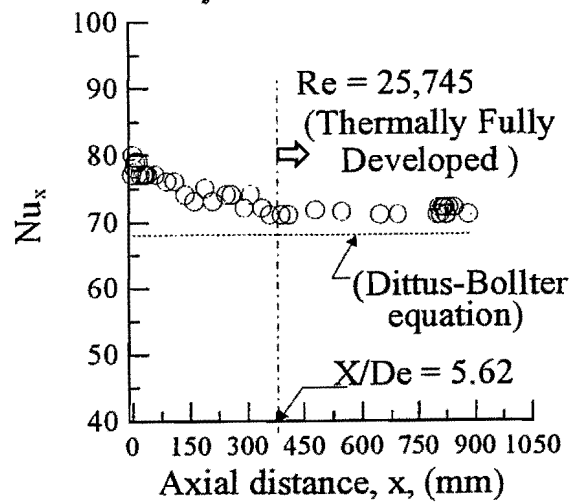


Fig. 8: Local Nusselt number versus axial distance in smooth rectangular duct, $Re = 25,745$.

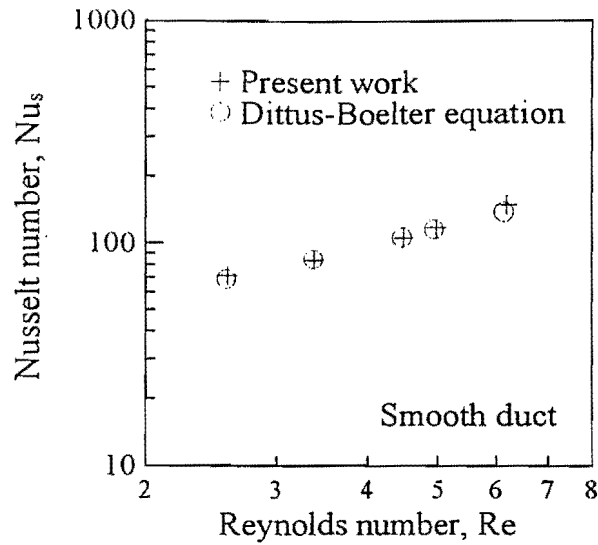


Fig. 9: Comparison of average Nusselt number for fully developed turbulent flow through present smooth duct and previously published results for circular tubes.

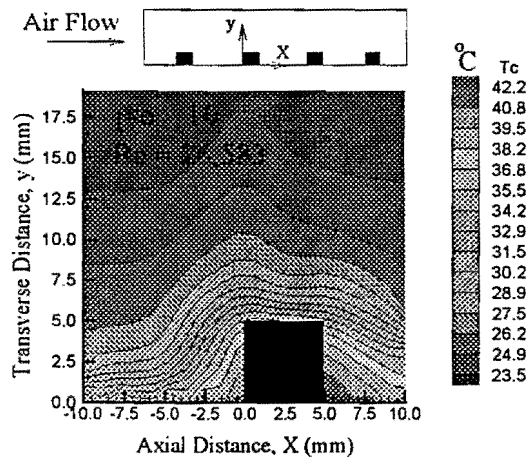


Fig. 10a: Local temperature distribution around the solid square rib for one ribbed-wall ($Re = 26,583$, $p/e = 10$).

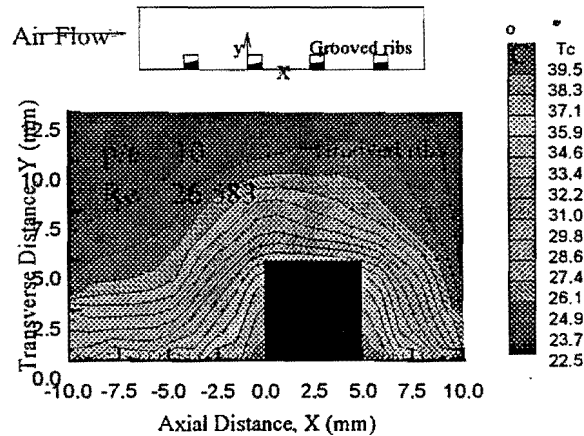


Fig. 10b: Local temperature distribution around the square grooved rib for one ribbed-wall ($Re = 26,583$, $p/e = 10$).

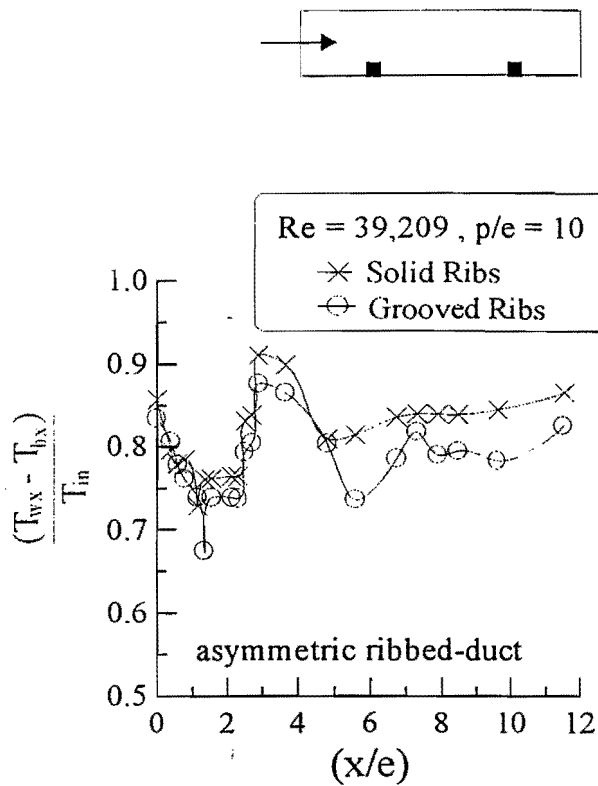


Fig. 11: Variation of dimensionless local wall temperature distributions versus dimensionless axial distance for asymmetric ribbed-duct with solid rib and grooved rib types ($p/e=10$).

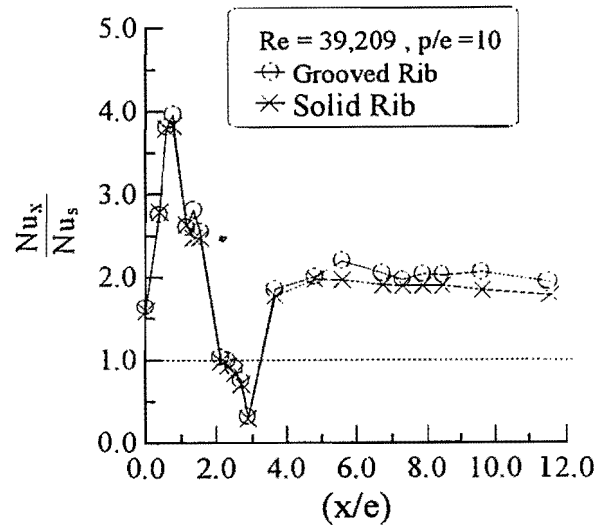


Fig. 12: Variation of local Nusselt number ratio distributions versus dimensionless axial distance for asymmetric ribbed-duct With solid and grooved rib types ($p/e=10$)

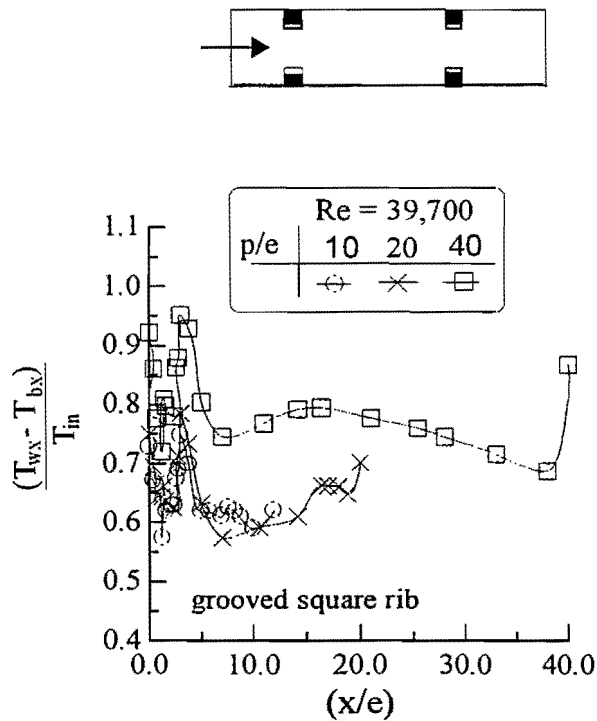


Fig. 13: Variation of dimensionless local wall temperature distributions versus dimensionless axial distance at different rib pitches for symmetric ribbed-duct with square grooved rib, $Re = 39,700$.

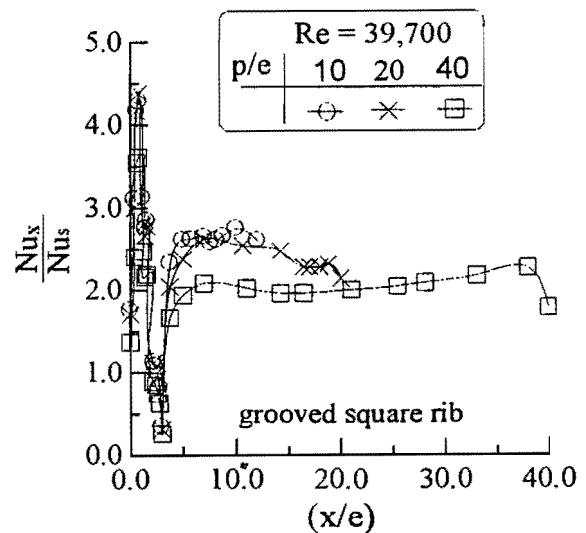


Fig. 14: Variation of local Nusselt number ratio distributions versus dimensionless axial distance at different rib pitches for symmetric ribbed-duct with grooved-rib

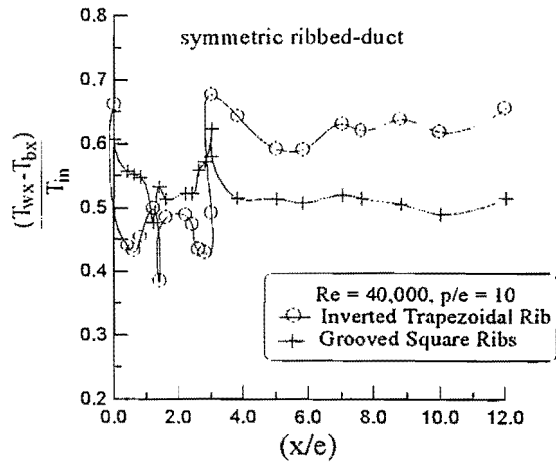


Fig. 15: Variation of dimensionless local wall temperature distributions versus dimensionless axial distance for symmetric ribbed-duct with different rib shapes, ($Re = 40,000$, $p/e = 10$).

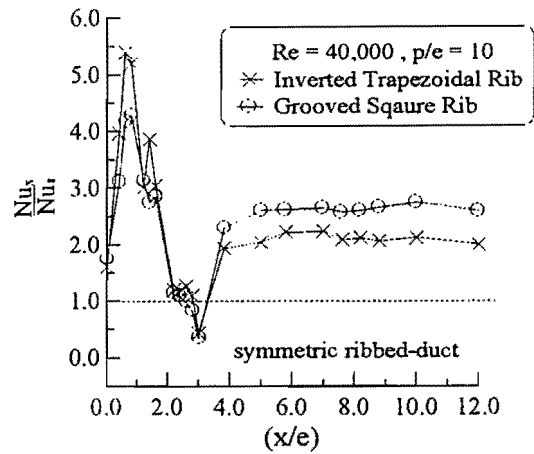


Fig. 16: Variation of local Nusselt number ratio distributions versus dimensionless axial distance for symmetric ribbed-duct with different rib shapes, ($Re = 40,000$, $p/e = 10$).

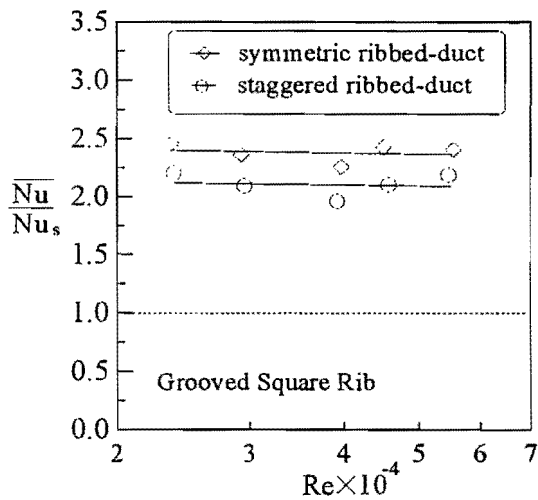


Fig. 17: Effect of Reynolds number on the average Nusselt number ratio for two ribbed-walls with square grooved ribs with different rib alignments, ($p/e = 20$).

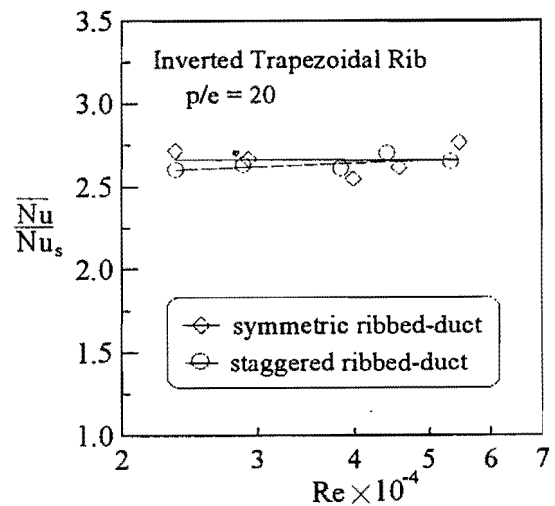














Fig. 18: Effect of Reynolds number on the average Nusselt number ratio for two ribbed-walls with inverted trapezoidal ribs with different rib alignment, ($p/e = 20$).

Constraint	Equal pumping power			Equal mass flow rate		
p/e	10	20	40	10	20	40
Inv. Trapezoidal						
Grooved Square						

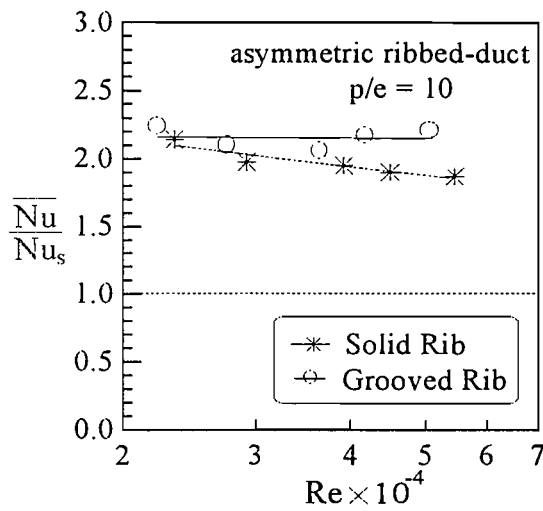


Fig. 19: Effect of Reynolds numbers on the average Nusselt number ratio for asymmetric ribbed-duct with solid and grooved square ribs, ($p/e = 10$).

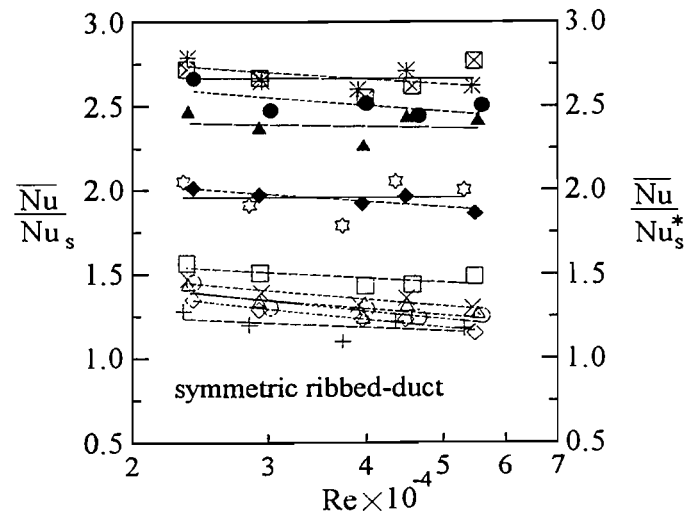


Fig. 20: Effects of rib shape, rib pitch, and Reynolds number on the average Nusselt number ratio under the two constraints through symmetric ribbed-duct.

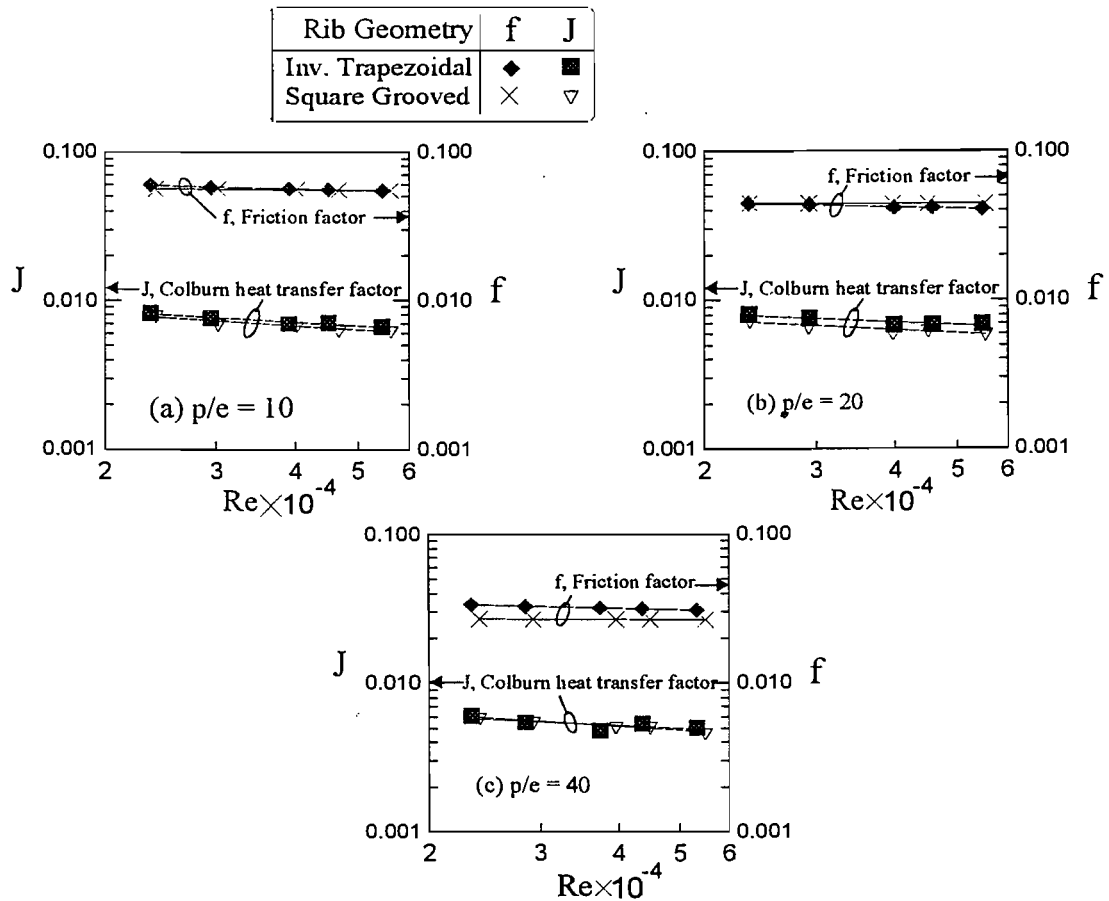


Fig. 21: Effect of Reynolds number on friction factor and Colburn factor for symmetric ribbed-duct with different rib shapes as well as different pitch to height ratios.

Rib Geometry	$p/e = 10$	
Inv. Trapezoidal	\circ	Present Exp. Work
Grooved Square	\diamond	
Solid Square	\blacktriangle	Liou et al., 1992 (part2)
Triangular	\times	
Semi-circular	\square	

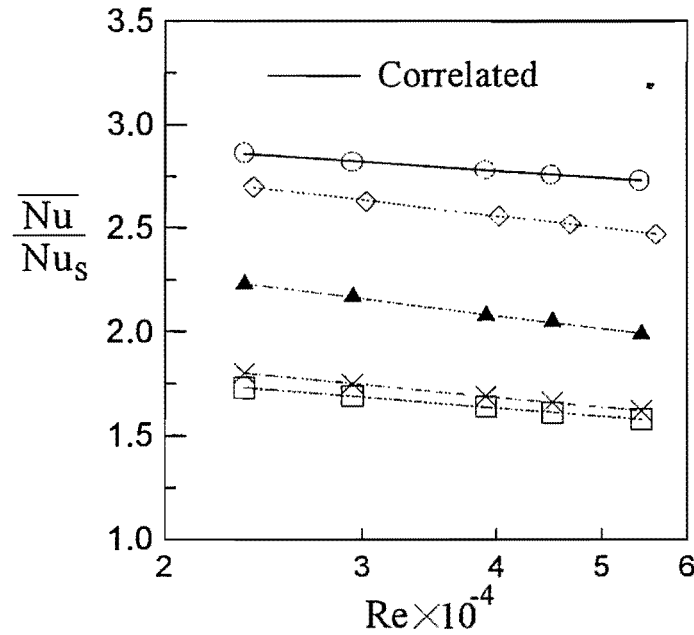


Fig. 22: Comparison of average Nusselt number ratio between the present experimental correlations in Eq. (1) and the previous correlations for different rib shapes ($p/e=10$, $e/D = 0.081$).

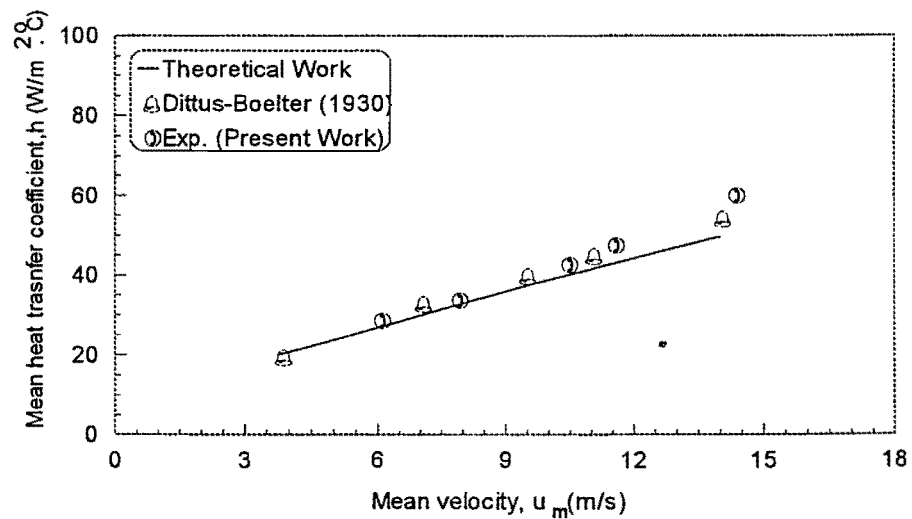
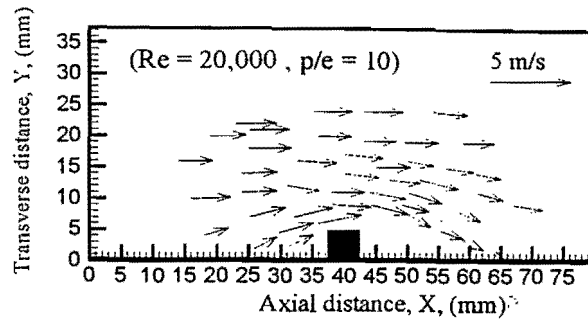
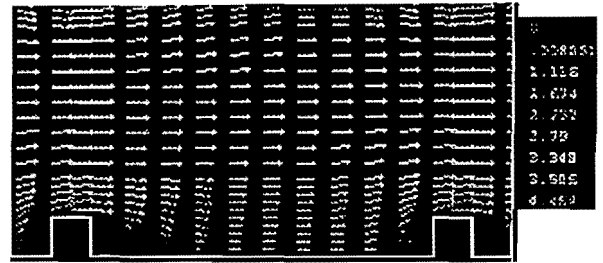


Fig. 23: Comparison of heat transfer coefficient between present experimental and numerical results and previously published results at different mean velocities.

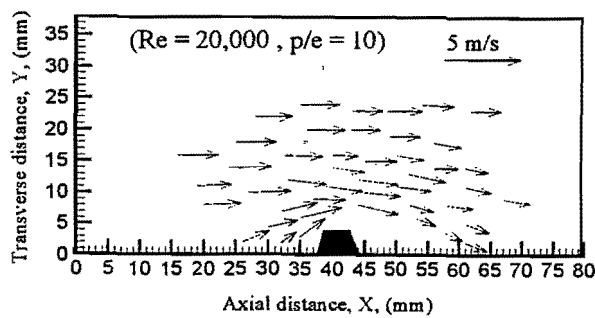


Experimental



Computed

a)- Square Rib

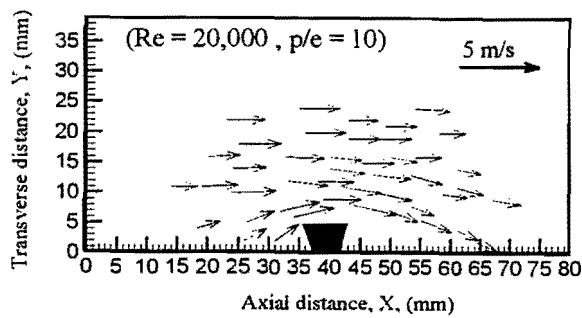


Experimental

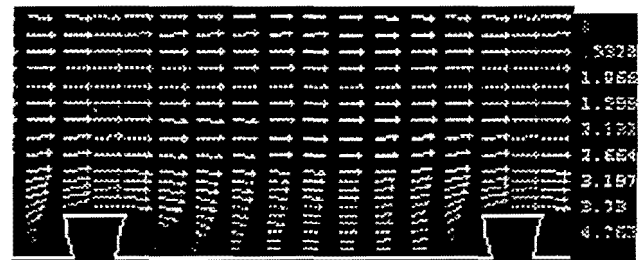


Computed

b)- Trapezoidal Rib



Experimental



Computed

c)- Inverted Trapezoidal Rib

Fig. 24: Comparison of velocity vectors between present measured and computed results in the test field around asymmetric rib alignment with different shapes, ($Re = 20,000$, $p/e = 10$).

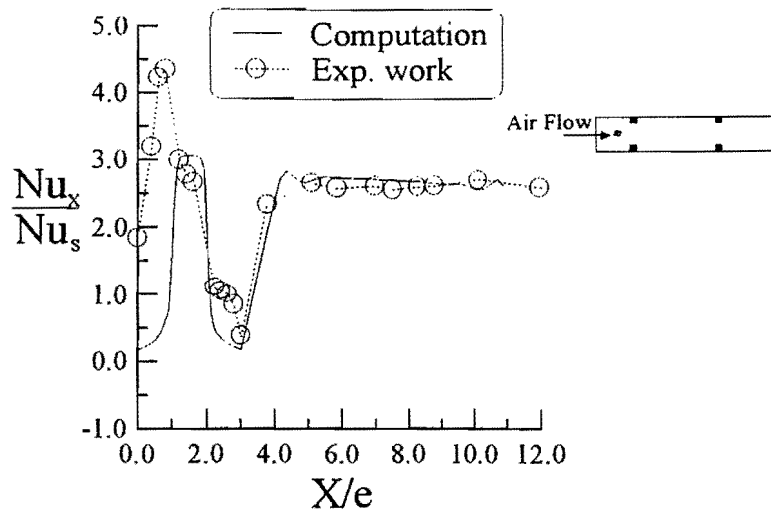


Fig. 25: Comparison of local Nusselt number ratio between measured and computed results for fully developed turbulent flow through symmetric ribbed-duct with solid square ribs ($p/e = 10$, $e/D_e = 0.081$, $Re = 27,313$).

$p/e = 10$	Rib Geometry	
	Solid Square	Inverted Trapezoidal
Present Exp. Work		○
Computed	—

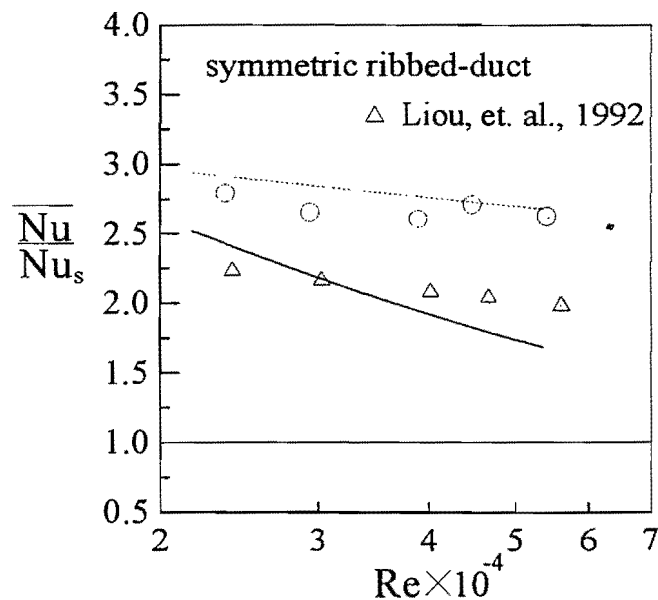


Fig. 26: Comparison of average Nusselt number ratio between measured and computed results for fully developed turbulent flow through symmetric ribbed-duct with different rib shapes ($p/e = 10$, $e/D_e = 0.081$, $Re = 27,313$).